HAL open science

Burton's Curse: The Impact of Bulk Flows on the Galactic Longitude–Velocity Diagram and the Illusion of a Continuous Perseus Arm

J. Peek, Kirill Tchernyshyov, Marc-Antoine Miville-Deschênes

▶ **To cite this version:**

J. Peek, Kirill Tchernyshyov, Marc-Antoine Miville-Deschênes. Burton's Curse: The Impact of Bulk Flows on the Galactic Longitude–Velocity Diagram and the Illusion of a Continuous Perseus Arm. The Astrophysical Journal, 2022, 925 (2), pp.201. 10.3847/1538-4357/ac3f34 . hal-03873389

HAL Id: hal-03873389

https://hal.science/hal-03873389v1

Submitted on 27 Nov 2022

HAL is a multi-disciplinary open access archive for the deposit and dissemination of scientific research documents, whether they are published or not. The documents may come from teaching and research institutions in France or abroad, or from public or private research centers.

L'archive ouverte pluridisciplinaire **HAL**, est destinée au dépôt et à la diffusion de documents scientifiques de niveau recherche, publiés ou non, émanant des établissements d'enseignement et de recherche français ou étrangers, des laboratoires publics ou privés.

Distributed under a Creative Commons Attribution 4.0 International License

The Astrophysical Journal, 925:201 (10pp), 2022 February 1 https://doi.org/10.3847/1538-4357/ac3f34
© 2022. The Author(s). Published by the American Astronomical Society.
OPEN ACCESS

Burton's Curse: The Impact of Bulk Flows on the Galactic Longitude–Velocity Diagram and the Illusion of a Continuous Perseus Arm

J. E. G. Peek[1,2], Kirill Tchernyshyov[3], and Marc-Antoine Miville-Deschenes[4]
[1] Space Telescope Science Institute, 3700 San Martin Drive, Baltimore, MD 21218, USA; jegpeek@stsci.edu
[2] Department of Physics & Astronomy, Johns Hopkins University, Baltimore, MD 21218, USA
[3] Department of Astronomy, University of Washington, Seattle, WA, USA
[4] AIM, CEA, CNRS, Université Paris-Saclay, Université Paris Diderot, Sorbonne Paris Cité, F-91191 Gif-sur-Yvette, France
Received 2021 July 29; revised 2021 November 29; accepted 2021 November 30; published 2022 February 4

Abstract

In this work, we demonstrate that the Perseus Arm is not a continuous structure of molecular gas in the second quadrant. We first show that the observed, distanced-resolved velocity structure of the Galaxy in the outer disk is capable of creating illusory spiral arms, as was first proposed by Burton. Second, we measure the distances to a collection of CO clouds at velocities consistent with the Perseus arm with $135° < l < 160°$. We find these distances using 3D dust maps from Green et al. We determine that these molecular clouds do not preferentially lie at the distance of a purported Perseus arm but rather extend over 3 kpc in distance, with some evidence for a closer, high pitch angle structure between 1 and 1.5 kpc away. Finally, we demonstrate that velocity perturbations of the amplitude found near the Perseus arm can wreak havoc on our interpretation of the longitude–velocity diagram for more than half of the Milky Way disk.

Unified Astronomy Thesaurus concepts: Milky Way dynamics (1051); Milky Way disk (1050); Milky Way rotation (1059); Spiral arms (1559); Interstellar medium (847)

1. Introduction

Much of the star formation in disk galaxies happens in their spiral arms, and thus understanding the spiral structure is key to understanding the process of star formation on large scales. On the other hand, we know star formation to be mediated by very small-scale stellar feedback and turbulent processes, which can be studied in the most detail within the Milky Way. Thus, understanding the true nature of the Milky Way spiral structure is critical to connecting the environment of star formation to its eventual result.

While our need to accurately map the Milky Way spiral structure has long been recognized, our location within the Milky Way disk limits our ability to discern the distances to the molecular clouds and star-forming regions that make up spiral arms. Emission tracers of the ionized, atomic, and molecular gas that make up the arms contain no intrinsic distance information, and stellar structures embedded within the arms are often obscured by intervening material. Even Gaia's state-of-the-art, large-scale precise parallactic distance information to individual stars is largely limited to nearby ($\lesssim$2 kpc), relatively unobscured, and unconfused regions (Gaia Collaboration et al. 2018). Very Long Baseline Array (VLBI) parallax measurements toward high-mass star formation regions (HMSFRs) provide a much more limited set of stellar distances, but one that is unaffected by dust and traces the star-forming regions of interest (Reid et al. 2014; Reid14).

Historically, astronomers have estimated distances to gas seen in emission by taking advantage of the analytic relationship between the distance and radial velocity that is created by the differential rotation of the Milky Way disk (van de Hulst et al. 1954). In particular, in the outer Milky Way there is a one-to-one, monotonic relationship between the distance and velocity that, under the assumption of a known and unperturbed rotation curve, allows us to exactly map out the structure of the disk beyond the solar circle (Levine et al. 2006, Kalberla & Kerp 2009; Miville-Deschênes et al. 2017a). This method represents one of the only ways to connect individual regions of star formation (as traced by, e.g., HMSFRs) into larger spiral structures across the Galactic disk. This linking is very important, as the pitch angle and continuity of the spiral structure is a key discriminant between different theories of spiral arm formation and persistence (Reid14).

Burton (1971; B71) examined this velocity-based map-making method and pointed out a fundamental flaw. By modeling a *completely smooth* interstellar medium (ISM) with the velocity field implied by the Lin et al. (1969) spiral structure density wave theory, B71 was able to reproduce many of the observed features in the Galactic H I longitude–velocity diagram. The implication of this work is that realistic spiral structure *velocity fields* generate perturbations to the longitude–velocity diagram that mimic in shape and amplitude those generated by spiral arm density fluctuations themselves. Burton & Bania (1974) followed up on this analysis, comparing distances to star clusters to the implied distances from velocities in H I. While these original theories of spiral structure are by no means the only ones under consideration for the Milky Way, recent work has shown that the Milky Way does indeed host line-of-sight velocity fluctuations of more than 10 km s^{-1} stretching for many kpc, which may be capable of generating these kinds of distortions (Tchernyshyov & Peek 2017; Tchernyshyov et al. 2018; TPZ18).

The Perseus arm in the outer Milky Way has long been used as a test bed for theories of the spiral structure, as it is (a) a purported nearby spiral arm, (b) in the outer Galaxy, (c) easily visible in the north, and (d) seemingly continuous across a large swath of the Galactic disk. Early work argued that the velocity and density field in this region was consistent with the two-arm

Original content from this work may be used under the terms of the Creative Commons Attribution 4.0 licence. Any further distribution of this work must maintain attribution to the author(s) and the title of the work, journal citation and DOI.

spiral shock model of the spiral structure (Roberts 1972). Subsequent observations of the positions and motions of gas and stars in the Perseus arm have also been found to agree with the Roberts (1972) model (Burton & Bania 1974; Humphreys 1976; Sparke & Dodd 1978; Wouterloot & Habing 1985; Sakai et al. 2019), though often with caveats. Humphreys (1976) found that the line-of-sight velocities of supergiant stars have the right signs but twice the expected amplitude. Sparke & Dodd (1978) noted the Perseus arm gap discussed in this paper but concluded that it could in fact be the result of a nonlinear effect hypothesized to occur in the spiral shock model. Sakai et al. (2019; Sakai19) found that the 3D velocities of HMSFRs in the Perseus arm are consistent with the Roberts (1972) model, but that HMSFRs in the rest of the purported spiral arms are not consistent with spiral shock-like models. The development of other theories of spiral structure continued, in particular variations on swing amplification (Toomre 1981; Sellwood & Carlberg 1984). Unlike the model by Roberts (1972), these models did not make the sort of explicit predictions for the Perseus arm and so were typically not compared with observations.

TPZ18 showed that the velocity fields around Perseus star-forming regions are inconsistent with these kinds of long-lived persistent spiral models and that material arm models, in which spiral arms are created and destroyed on less than a winding time, are more consistent with the observed velocity fields. These material arm models are incapable of making long, shallow pitch angle spiral arms, which stands in contradiction to the observed length and tight winding in the Perseus arm as identified in the longitude–velocity diagram. Here, a shallow pitch angle refers to the small angle made by the arm and a constant radius circle (see, e.g., Sellwood & Masters 2021). New observations of hot stars, Cepheids, and open clusters mined from Gaia EDR3 (Gaia Collaboration et al. 2021) also seem to show a more loosely wound Perseus arm (Poggio et al. 2021). Longer, more tightly wound spiral arms, as argued for in Reid14, rely on sparse HMSFRs linked together by features in the molecular (CO) and atomic (H I) longitude–velocity diagrams. While the distances and velocities of HMSFRs are not in doubt, can we really trust the links between them, or are they an illusion, as described in B71?

In this work, we put the Perseus arm to the test, examining whether a key part of this arm is indeed contiguous, or rather an illusion generated by Galactic velocity fields, as described in B71. The part of Perseus we examine here does not have any known masers but is important in connecting star-forming regions in the second and third quadrants and thus establishing the shallow pitch angle of the purported arm. In Section 2, we describe the 3D dust maps, CO, H I, and HMSFR maser data we use. In Section 3, we show how previously measured radial velocity fields provide the possibility of spiral arm illusions in the Perseus arm and describe our method for measuring the distance to individual molecular clouds in this region. In Section 4, we discuss the implications of our measured distance distribution of molecular clouds in the region under consideration, and we conclude in Section 5.

2. Data

2.1. 3D Dust Maps

We use the 3D dust data products described in Green et al. (2019; G19). In brief, G19 uses the optical and near-IR photometry of 799 million stars, along with their Gaia data release 2 (Gaia Collaboration et al. 2018) parallax measurements, to infer the combinations of the stellar type, distance, and foreground reddening that are possible for each star. By combining these probability distribution functions for all stars near each line of sight, G19 produced a 3D dust map, with typical angular resolution 3.′4, and distance bins of 0.125 distance moduli. We will refer to the total reddening profile along the line of sight from this map as $E(B-V)(d)$ and to the radial differential reddening profile as $\Delta E(B-V)(d)$. Adjacent bins are somewhat correlated, as a smooth spatial prior is applied in an iterative scheme to the map. Five realizations of the map are provided, and we access them using the *dustmaps* code (Green 2018). Additionally, each pixel in the map is labeled with its maximum and minimum reliable distances; lines of sight with few stars or opaque clouds cannot reliably return dust information beyond a certain point.

We note that G19 finds that the Reid14 HMSFRs are associated with regions of dense dust, but that there is no clear evidence for the kind of shallow pitch angle spiral structure found in Reid14 in the G19 dust maps themselves. We believe this result is consistent with what we find in this work.

2.2. Kinetic Tomography

In order to show that the true velocity field of the Milky Way is capable of producing the significant velocity crowding effects described in B17, we use the kinetic tomography map published in TPZ18. TPZ18 used the 1.53 μm diffuse interstellar band absorption feature in stars from the Apache Point Observatory Galactic Evolution Experiment (Zasowski et al. 2015; Majewski et al. 2017) to measure the velocity field across the Milky Way disk in the first three quadrants within about 4 kpc. These maps confirmed the overall results of the previous maps (Tchernyshyov & Peek 2017; TP17), which showed that there are bulk flows of material in the Galaxy that can stretch many kpc at tens of km s^{-1} beyond what is expected from Galactic rotation. Additionally, we use the results of TP17 as an illustration of our results in Section 4.

2.3. ISM Gas Tracer Observations

We use the compilation of 21 cm hydrogen (H I) and microwave carbon monoxide (CO) observations described in TP17 to provide a template for contaminating reddening, as described in Section 3.2. Practically speaking, this means we used CO observations from (Dame et al. 2001; DHT01) and H I observations from Kalberla et al. (2005).

2.4. Cloud Identification

To select individual molecular clouds, we used the decomposition of the DHT01 map provided by Miville-Deschênes et al. (2017a; MML17). MML17 used a hierarchical cluster identification method to collect Gaussian velocity components of the DHT01 CO survey into a list of 8246 molecular clouds across the Galactic disk. The data contain both a list of the 8246 clouds and their bulk properties but also a list of the individual Gaussian components associated with each cloud. This augmented and slightly modified MML17 data set is described in Appendix and can be found at https://doi.org/10.7910/DVN/QR9CFW.

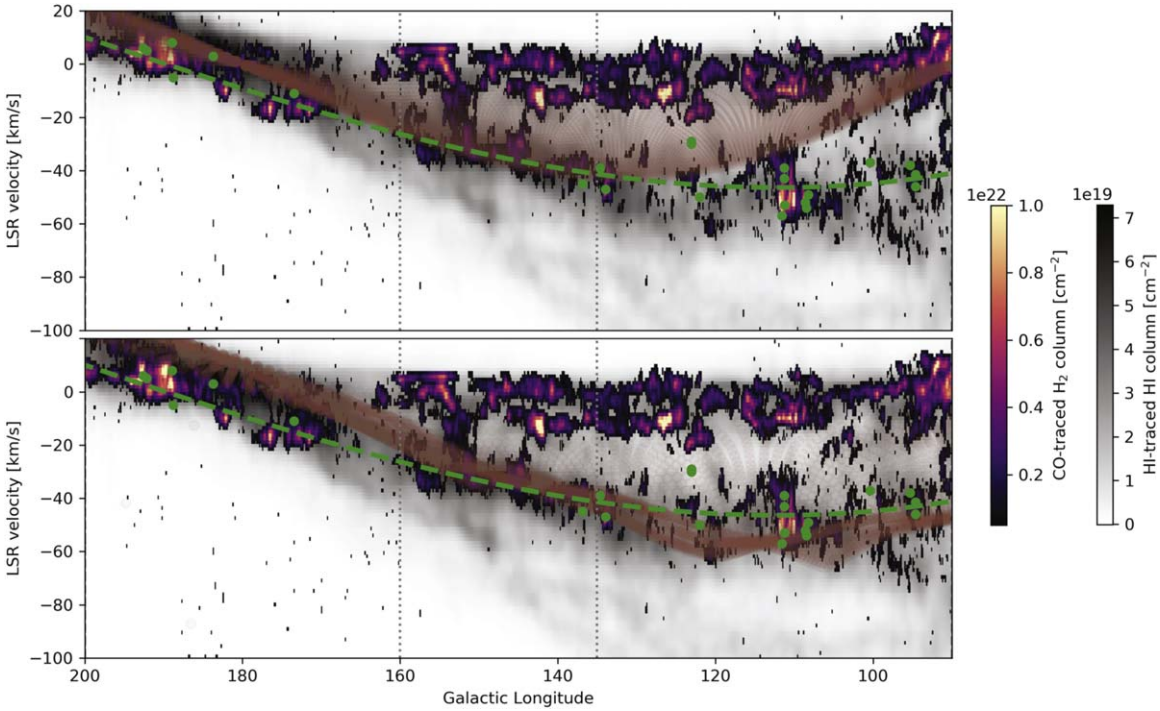

Figure 1. The Galactic longitude–velocity diagram in the Galactic midplane ($b = 0$). For each panel, the H I column is shown in grayscale, and the CO column is shown in the "magma" color map. The bounds of the regions we focus on in Section 3.2 are marked by dotted gray lines. The velocity track of the **purported** Perseus arm is denoted by the dashed green line (Choi et al. 2014). Masers from Reid14 and Sakai19 are shown as green dots. Overplotted in brown is a representation of a perfectly smooth ISM. The brown points are smoothly distributed over the Galactic disk within 4 kpc, projected using a flat rotation curve (top) and the velocity field derived in Tchernyshyov et al. (2018) (bottom). This figure shows that track of the Perseus arm can be generated by the velocity field derived in Tchernyshyov et al. (2018) without density fluctuations.

2.5. High-mass Star Formation Regions

Finally, we also use the HMSFRs compiled in Reid14 and Sakai19. This represents the largest single collection of HMSFRs with parallactic distances ever assembled. These targets are very helpful for studying the global structure of star formation in the Milky Way because they are found in areas of active star formation and contain masers, whose parallaxes (and hence distances) and radial velocities can be measured accurately using VLBI. This combination is very powerful for tracing out the spatial and velocity structure of the Milky Way's star-forming disk.

3. Methods and Analysis

In this section, we develop methods and conduct analyses in pursuit of answers to two questions. First, does the previously measured velocity field of the Milky Way in the outer Galaxy allow for an illusory spiral structure in the outer Milky Way? Second, if so, is the dense material in the velocity feature actually distributed over a much larger range of distances?

3.1. Illusory Spiral Structure is Possible

In B71 it was shown that, in the inner Galaxy, a significant spiral-like structure could be generated using the velocity field expected from the density-wave theory derived in Lin et al. (1969) with *no density variation at all*. While the idea of a perfectly smooth ISM is inconsistent with essentially every ISM observation, the analysis proved the point that "the profiles are more sensitive to small variations in the streaming motions than to small variations in the hydrogen density". This revelation was key to the movement toward studying CO as a tracer of the spiral arm structure rather than H I (R. Benjamin, private communication).

To verify this result, and thus demonstrate that velocity crowding in the Milky Way disk is possible, we apply the disk velocity field results of TPZ18 to a perfectly smooth disk. We lay down a smooth grid of points across the second quadrant out to a distance of 4 kpc, where we believe the TPZ18 map to be largely complete and accurate. Then, we perform two experiments. First, we use a standard flat, 220 km s^{-1} rotation curve to place each of these points at a velocity, as shown in panel 1 of Figure 1. Then, we use the radial velocity field as measured by TPZ18 to place these same smoothly distributed points on a second longitude–velocity diagram, as shown in panel 2 of Figure 1.

It is quite clear from these synthetic longitude–velocity diagrams that the Perseus arm in the second quadrant would be easily visible in the longitude–velocity diagram given the TPZ18 map of the velocity field and a perfectly smooth Galactic disk. While this "velocity crowding" situation provides the opportunity for illusory features in the longitude–velocity diagram, it does not mean that what we see in the maser-free sections of the Perseus arm is illusory. It is certainly possible that dense material also physically exists at these distances and that the velocity crowding is only piling on lower density, non-star-forming material at these velocities. Indeed, the HMSFRs from Reid14 and various maps of young stars (e.g., Xu et al. 2018) show that at least in some regions there do exist star-forming regions at the distance of the Perseus arm.

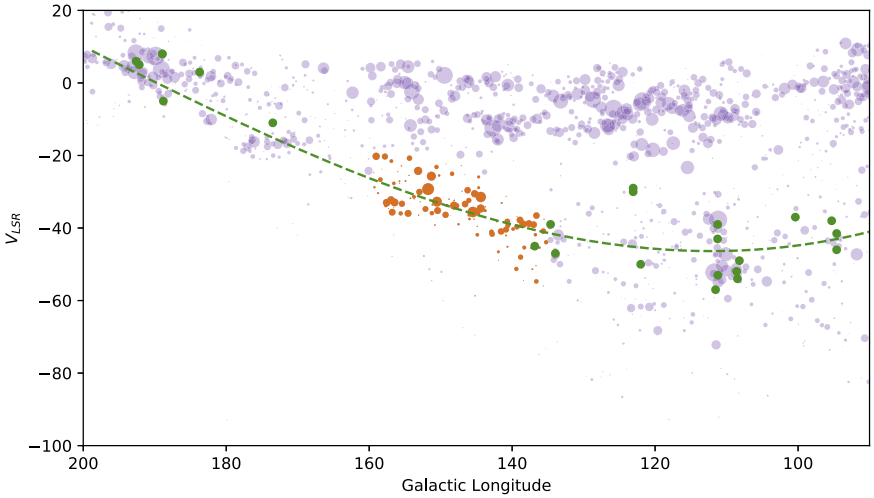

Figure 2. Circles represent CO clouds from MML17. CO clouds shown in orange represent the ones we investigate and in purple those not under investigation. Green dots are HMSFRs from Reid14 and Sakai19.

3.2. Illusory Spiral Structure Impacts the Perseus Arm Identification

In Section 3.1, we have shown that velocity fields observed in the outer Milky Way disk are sufficiently strong to create spiral arms in the longitude–velocity diagram in the absence of any density enhancements in the disk at all. To determine whether dense gas features are being erroneously connected into longer spiral structures in practice, we seek to measure the true distances to molecular clouds thought to reside in kinematic spiral arms. We focus our attention on the region between $l = 135$ and $1 = 160$ at velocities consistent with those in the Perseus arm.

We focus on this region because it contains no HMSFRs with parallactic distances and no evidence of young stars clustered at the expected distance Reid14, but has a very clear spiral feature in both H I and CO gas and is near enough ($\sim$2 kpc) that the G19 reddening map is generally trustworthy. If this feature exists only in the velocity space and not in the distance space, we believe there is currently no evidence of a continuous Perseus spiral arm across the second and into the third quadrant of the outer Galaxy.

First we select a sample of clouds from MML17, which are part of the visually identifiable Perseus arm. We constrain ourselves in the longitude: $135° < l < 160°$. Then we make overall constraints on the velocity: $-65\ \mathrm{km\ s^{-1}} < V_{\mathrm{LSR}} < -20\ \mathrm{km\,s^{-1}}$. Finally we fine-tune the velocity boundaries to follow the arm in the longitude–velocity space: $V_{\mathrm{LSR}}/\ \mathrm{km\ s^{-1}} < (l - 169°)/°$ and $0.6(V_{\mathrm{LSR}} + 35\ \mathrm{km\,s^{-1}})/\ \mathrm{km\ s^{-1}} > (l - 160°)/°$. These constraints result in 114 CO clouds, as shown in Figure 2. For each one of these clouds, we measure the distance using the G19 map. If the ISM consisted only of these clouds, the procedure for determining their distance would be relatively simple—measure the average $\Delta\mathrm{E(B-V)}(d)$ along the line of sight and find the peak. Works like Schlafly et al. (2014) and Zucker et al. (2020) have made very detailed studies of distances to clouds and subclouds using some of the techniques in G19, but these have typically been at closer distances or further off the plane. Unfortunately, there are many other structures along the line of sight, including the CO clouds in the very strong Local Arm between 0 and $-20\ \mathrm{km\,s^{-1}}$ (see Figure 1) and the more diffuse phases of the ISM along the line of sight not detected in DMT01.

To mitigate the effect of foreground ISM structures along the line of sight, we also choose a control region, which we call an "off", consisting of the area of sky more than 7 pixels away from any region of the cloud and less than 16 pixels in the DMT01 CO map (see left panels of Figure 3). Each pixel in the DMT01 map is 7.′5, such that the off region consists of an area roughly 1° to 2° from the cloud in question. For each of the cloud and off region, we find all the corresponding dust pixels in G19 that have complete data out to at least 4 kpc.

For both the cloud and the off region we make a weighting map consisting of the total column of material along the line of sight except for the cloud itself. To do this, we use the fiducial column density conversion factors for 21 cm H I and microwave CO 1–0 transitions (Bolatto et al. 2013):

$$N(\mathrm{H\,I}) = 1.8 \times 10^{18} \frac{\mathrm{T}_B d\nu}{\mathrm{K\ km\ s^{-1}}}, \tag{1}$$

and

$$X(\mathrm{CO}) = 2.0 \times 10^{20} \frac{\mathrm{T}_B d\nu}{\mathrm{K\ km\ s^{-1}}}. \tag{2}$$

We apply them to the CO and H I maps, sum them, and subtract the contribution from the cloud according to MML17. These maps allow us to weight our average measurement of the dust for the clouds and the offs by the inverse of the unrelated ISM column. This weighting allows us to focus on sightlines that are less contaminated by intervening and unrelated material, though in practice we find using an unweighted average does not change the conclusions of this work.

We look to estimate the distance to each cloud using the dust reddening measurements of G19. To compute this distance, we construct the difference between our on-cloud weighted $\Delta\mathrm{E(B-V)}(d)$ and the off-cloud weighted $\Delta\mathrm{E(B-V)}(d)$. In the very near field $d < 0.7$ kpc, we find that it is impossible to fully subtract the effects of the Local Arm material, which is very strong and quite variable. Thus, we focus our attention on the range $0.7\ \mathrm{kpc} < d < 5\ \mathrm{kpc}$ in our analysis. For each cloud, we find the interval over this distance range that captures 68.3% of the nonnegative cloud-off $\Delta\mathrm{E(B-V)}(d)$ that covers the least distance and use the center of this range as our distance estimator (see right panels of Figure 3). We find this method is much more resilient to the complex, non-Gaussian

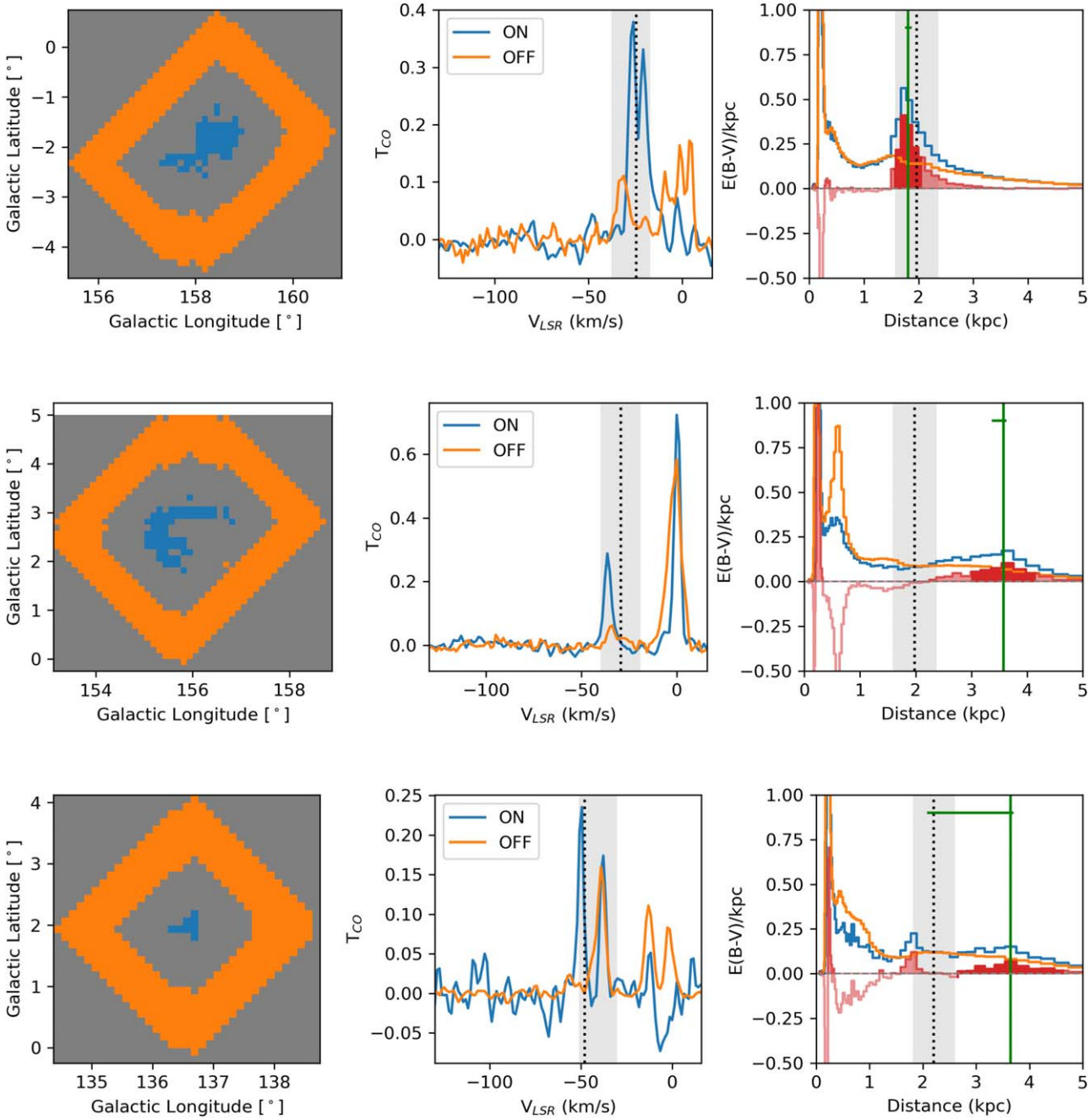

Figure 3. Three clouds demonstrating three main results from the analysis. The left column of panels shows the on region representing the clouds from MML17 (blue) and the "off" region in orange. The CO spectra representing these regions are shown in the second column, with the cloud velocity denoted by the black dotted line and the gray region representing the Perseus velocities. The third column shows the average reddening at each distance for the regions in blue and orange, and their difference in red, with the expected distance to the Perseus arm shown with the dashed black line. The top cloud is an example for which the method finds a result that is consistent with the expected distance of the arm, the middle cloud is a successful distance at an inconsistent distance, and the bottom cloud is an example for which the method fails.

distributions that are the result of the complex intervening ISM than, e.g., first moment measurements.

To measure errors, we turn to block bootstrapping. Standard bootstrap analysis (Efron 1982) is extremely useful for situations in which errors on samples are uncorrelated but otherwise quite complex. Unfortunately, while the errors in distance for this measurement are indeed complex (being totally dominated by intervening clouds rather than measurement noise), they are by no means independent; two adjacent pixels are very likely to be contaminated by the same intervening cloud. Thus, standard bootstrapping is both technically inapplicable and practically inaccurate. For this reason, we turn to block bootstrapping, a procedure of resampling with replacement, but for subregions (blocks) rather than individual pixels (Hall 1985).

To make subregions for a given region (cloud or off), we first find the average position of the region in Galactic coordinates. Then we compute a clock-angle on the surface of the sky for each of the pixels in the region around this center position. Finally, we divide the region into blocks based on the pixels clock-angle rank, with the largest block having no more than one extra pixel than the smallest block. This creates

Table 1
Clouds with Measured Dust Distances

Cloud Number	MML17 Cloud Number	l (°)	b (°)	V_{LSR} (km s^{-1})	Area (deg^2)	Av. Flux (K km s^{-1})	Dust Distance (kpc)
1	2168	137.65	1.41	−38.8	1.31	2.8	$1.92^{+0.09}_{-0.06}$
2	2178	136.60	1.17	−36.6	0.78	4.4	$1.86^{+0.09}_{-0.03}$
3	2182	148.13	0.25	−33.8	1.92	2.6	$1.39^{+0.03}_{-0.08}$
4	2190	144.39	−1.20	−31.4	2.27	3.7	$1.84^{+0.02}_{-0.16}$
5	2201	151.76	−1.19	−29.3	2.62	4.2	$2.12^{+0.09}_{-0.34}$
6	2702	136.75	1.10	−41.8	0.23	3.8	$2.20^{+0.31}_{-0.06}$
7	2712	137.00	1.37	−39.1	1.03	3.4	$1.76^{+0.09}_{-0.01}$
8	2731	145.50	0.86	−35.6	2.06	4.2	$1.26^{+0.03}_{-0.09}$
9	2736	150.52	−0.94	−32.7	3.20	2.4	$1.46^{+0.08}_{-0.06}$
10	2749	151.30	−0.53	−25.7	1.16	5.5	$2.31^{+0.12}_{-0.59}$
11	2757	150.58	−0.88	−23.2	0.41	3.6	$1.85^{+0.09}_{-0.35}$
12	3397	140.85	−1.17	−40.4	0.66	4.4	$1.15^{+0.26}_{-0.09}$
13	3398	141.56	−1.22	−41.0	1.86	1.7	$1.30^{+0.08}_{-0.05}$
14	3417	140.68	0.81	−38.2	1.30	2.0	$1.94^{+0.09}_{-0.06}$
15	3422	156.78	−1.85	−35.6	1.44	2.5	$1.51^{+0.03}_{-0.00}$
16	3429	144.80	1.01	−35.9	0.41	4.6	$1.23^{+0.08}_{-0.04}$
17	3430	146.03	1.01	−36.4	0.17	4.6	$1.20^{+0.16}_{-0.07}$
18	3436	156.95	−2.94	−32.3	1.52	2.9	$1.48^{+0.07}_{-0.04}$
19	3440	157.55	0.85	−33.0	1.91	2.4	$1.45^{+0.03}_{-0.06}$
20	3444	145.24	−1.08	−30.5	1.69	2.5	$1.32^{+0.24}_{-0.14}$
21	3454	146.24	1.25	−29.6	1.09	3.0	$1.28^{+0.03}_{-0.09}$
22	3477	154.37	−1.15	−20.7	0.91	2.6	$1.69^{+0.09}_{-0.45}$
23	4324	135.64	−0.13	−40.9	1.66	1.5	$2.28^{+0.05}_{-0.07}$
24	4338	142.80	−0.96	−41.7	1.80	1.4	$1.06^{+0.05}_{-0.02}$
25	4356	144.87	1.56	−41.9	0.55	1.9	$1.39^{+0.03}_{-0.06}$
26	4360	138.90	−0.41	−37.8	2.92	1.2	$2.66^{+0.04}_{-0.06}$
27	4363	139.87	0.29	−40.3	0.67	1.5	$1.46^{+0.22}_{-0.31}$
28	4386	150.43	0.42	−35.2	1.81	2.1	$1.53^{+0.03}_{-0.04}$
29	4388	151.23	0.73	−35.9	1.08	1.4	$3.39^{+0.06}_{-0.34}$
30	4394	152.13	1.57	−34.8	2.05	1.3	$3.43^{+0.07}_{-0.08}$
31	4396	155.59	2.54	−36.0	0.97	1.5	$3.58^{+0.03}_{-0.19}$
32	4402	147.78	−0.53	−33.9	1.25	1.9	$1.32^{+0.10}_{-0.07}$
33	4403	156.45	−0.37	−33.0	3.52	1.4	$1.38^{+0.05}_{-0.07}$
34	4404	151.16	−0.32	−33.6	0.11	2.4	$2.44^{+0.16}_{-0.19}$
35	4407	149.11	−0.16	−33.8	0.41	1.8	$1.53^{+0.03}_{-0.15}$
36	4409	149.31	0.75	−36.4	1.98	1.6	$1.56^{+0.05}_{-0.04}$
37	4410	146.58	0.47	−33.4	1.61	2.1	$1.39^{+0.03}_{-0.12}$
38	4414	155.42	1.35	−33.3	2.11	1.4	$1.55^{+0.36}_{-0.10}$
39	4417	157.68	1.80	−33.8	0.78	1.2	$1.58^{+0.04}_{-0.06}$
40	4427	152.97	−0.85	−30.1	1.66	1.9	$2.60^{+0.03}_{-0.24}$
41	4461	158.44	−1.98	−26.7	0.91	1.9	$1.81^{+0.04}_{-0.03}$
42	4463	148.40	−1.58	−25.0	1.05	1.5	$1.89^{+0.13}_{-0.09}$
43	4476	153.15	−1.55	−24.3	2.08	2.5	$1.76^{+0.06}_{-0.04}$
44	4494	157.80	−2.24	−20.3	1.44	2.1	$1.79^{+0.07}_{-0.03}$
45	4495	159.02	−2.30	−20.2	1.88	2.3	$2.04^{+0.01}_{-0.08}$
46	4496	156.89	−2.35	−21.5	0.55	2.0	$1.51^{+0.04}_{-0.03}$
47	5877	136.62	0.29	−54.7	1.09	1.5	$2.15^{+0.07}_{-0.06}$
48	5892	145.19	2.83	−58.7	0.14	1.0	$4.12^{+0.12}_{-0.98}$
49	5909	135.63	1.81	−55.9	0.08	0.9	$3.78^{+0.17}_{-0.27}$
50	5935	138.82	−1.83	−48.0	1.19	1.8	$1.12^{+0.08}_{-0.01}$
51	5954	137.17	3.12	−51.4	0.20	1.2	$3.98^{+0.09}_{-0.38}$
52	5960	152.34	−0.70	−47.7	0.16	0.9	$2.30^{+0.06}_{-0.22}$
53	5981	138.30	−0.75	−45.4	1.02	1.2	$2.74^{+0.06}_{-0.04}$
54	5988	140.66	0.32	−45.2	0.28	1.1	$1.71^{+0.04}_{-0.10}$
55	6000	136.18	2.12	−45.4	0.48	1.1	$4.32^{+0.04}_{-0.16}$
56	6047	141.21	1.58	−40.6	0.09	1.0	$1.81^{+0.08}_{-0.13}$
57	6057	147.50	−2.28	−39.0	0.42	1.0	$1.52^{+0.09}_{-0.27}$

Table 1
(Continued)

Cloud Number	MML17 Cloud Number	l (°)	b (°)	V_{LSR} (km s^{-1})	Area (deg^2)	Av. Flux (K km s^{-1})	Dust Distance (kpc)
58	6070	145.96	2.62	−37.5	0.47	1.1	$3.94^{+0.18}_{-0.20}$
59	6074	142.15	3.31	−38.2	0.27	0.8	$2.01^{+0.05}_{-0.32}$
60	6078	143.78	−3.38	−35.2	0.17	4.2	$1.07^{+0.07}_{-0.10}$
61	6097	144.88	2.34	−39.5	0.12	1.1	$4.17^{+0.08}_{-0.23}$
62	6103	148.12	−2.35	−32.4	0.12	1.7	$1.74^{+0.07}_{-0.08}$
63	6125	148.82	2.11	−32.0	0.12	1.5	$1.65^{+0.06}_{-0.22}$
64	6131	157.30	2.88	−34.7	0.08	1.2	$3.35^{+0.33}_{-0.17}$
65	6135	154.24	−0.91	−31.8	0.23	1.0	$1.88^{+0.01}_{-0.59}$
66	6142	158.75	0.01	−30.4	0.39	0.9	$0.99^{+0.17}_{-0.09}$
67	6143	152.87	0.22	−32.8	0.14	0.8	$2.43^{+0.16}_{-0.09}$
68	6155	156.55	2.45	−27.7	0.94	1.0	$3.50^{+0.07}_{-0.06}$
69	6163	155.74	−2.73	−27.6	0.08	1.2	$1.84^{+0.09}_{-0.08}$
70	6164	147.01	−2.44	−29.8	0.09	1.2	$1.10^{+0.10}_{-0.03}$
71	6165	154.91	−2.03	−27.0	0.22	1.2	$1.88^{+-0.01}_{-0.25}$
72	6170	155.76	−1.22	−27.1	0.30	0.8	$1.52^{+0.03}_{-0.09}$
73	6171	159.26	−0.85	−28.8	0.53	0.8	$1.33^{+0.33}_{-0.12}$
74	6183	150.21	−2.51	−25.5	0.38	1.3	$1.39^{+0.29}_{-0.10}$
75	6185	156.00	−2.41	−24.5	0.09	1.1	$1.46^{+0.14}_{-0.04}$
76	6222	159.36	0.88	−24.7	0.09	0.9	$0.93^{+0.12}_{-0.07}$
77	6238	147.11	−2.34	−22.8	0.08	1.1	$1.22^{+0.23}_{-0.10}$
78	6240	155.49	−1.88	−22.9	0.19	0.9	$1.55^{+0.09}_{-0.01}$
79	9099	138.41	3.42	−54.5	0.08	0.8	$3.95^{+0.10}_{-0.30}$
80	9139	153.68	1.54	−32.0	0.08	0.8	$1.42^{+0.32}_{-0.17}$

largely contiguous blocks of pixels of equal size. We use 12 blocks for each region. As we perform this block bootstrap, we also bootstrap on the five realizations of the dust map. We find that the map realization bootstrapping adds very little to the overall errors, which is consistent with our expectation that intervening clouds, and not measurement noise, are our largest source of uncertainty.

While we have built a system to find cloud distances that is as robust as possible in the presence of intervening material, some clouds are too small or too obscured to find with this method. First, we reject 26 additional clouds for having a $\pm 1\sigma$ error range that is more than a factor of 1.5 in distance. Second, we reject 8 clouds for having very heavy-tailed dust profiles, defined by having a 68.3% ($\pm 1\sigma$) interval 3.5 times larger than their 38.3% ($\pm 0.5\sigma$) interval or having a 86.6% ($\pm 1.5\sigma$) interval 3.5 times larger than their 68.3% interval. This leaves us with a sample of 81 out of 114 initial clouds, which we report in Table 1 and map in Figure 4. We note that this procedure makes it clear that we are biased away from finding the most distant clouds, as they tend to be fainter and smaller overall. We expect that this sample is thus more complete closer to the Sun. We see in Figure 4 that the bulk of CO clouds at the Perseus arm velocity in this longitude range are not consistent with being at the distance of the Perseus arm. The longitude–velocity diagram of the Perseus arm is shown with distances assigned in Figure 5, clearly demonstrating a very wide range of distances for clouds very near each other in the velocity space.

4. Discussion

Section 3.1 and Figure 1 show that the velocity field toward the Perseus Arm in the second quadrant of the Milky Way is able to produce the structure-emulating velocity crowding effect discussed by Burton (1971). From Section 3.2 and Figure 4, we can see that this velocity crowding is indeed solely responsible for the bridge of molecular clouds that connect star-forming regions at $l \simeq 140°$ to those in the anticenter in the longitude–velocity diagram. From this analysis, we find no evidence of any kind of overdensity of molecular clouds at the distance of the Perseus arm over this range in longitude. The analyses conducted in Section 3.1 and Section 3.2 produce consistent results, in that clouds in the Perseus component of the longitude–velocity diagram are actually distributed over a very large range of distances. Indeed, the clouds generally line up with the sample of O and B stars described in Xu et al. (2018). This result is consistent with the lack of evidence for a stellar overdensity in this region in Poggio et al. (2021). Further, the wedge of molecular clouds we find closer than the purported Perseus arm is somewhat consistent with the "Cepheus Spur" of young stars highlighted most recently in Pantaleoni González et al. (2021), although we note that the overlap is not complete. In Figure 5, the impact of velocity crowding is made clear; clouds with very different distances can be put at very similar places in the longitude–velocity diagram. The velocity bridge we have interrogated here is, to our knowledge, the only connection between the star-forming region that ends at $l \simeq 135°$ and the cluster near-Galactic anticenter, $l \simeq 180°$. Additionally, we show the cloud distance results in the distance–velocity space broken up over five regions of Galactic longitude in Figure 6. In this figure. we include the velocities derived in TP17 to illustrate both how the final results of this work are consistent with TP17 and how many distances correspond to the same narrow range of velocities over many sightlines. This figure very clearly shows that it is very difficult to directly relate a velocity to a distance

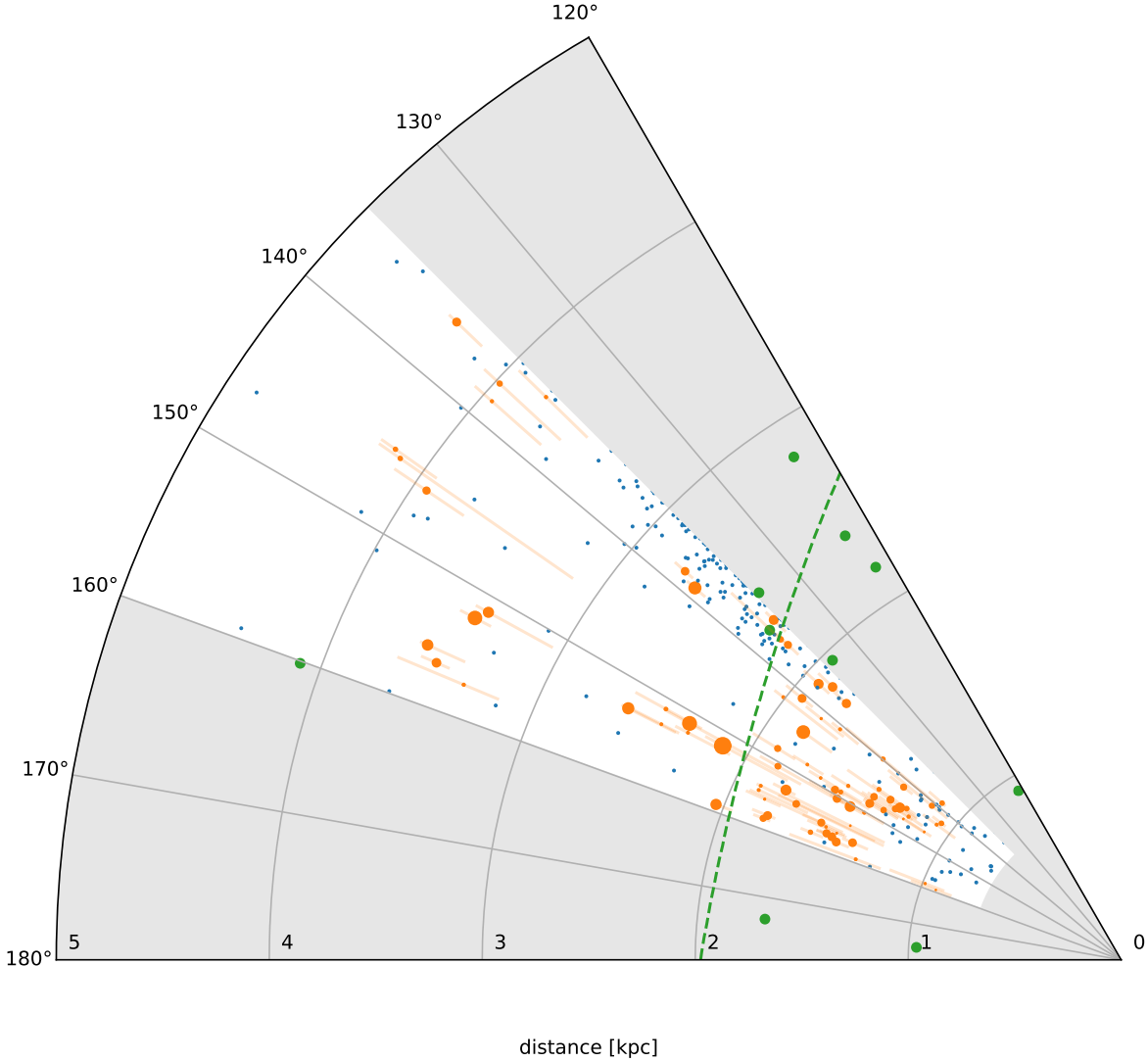

Figure 4. Distribution of 81 MML17 clouds determined by reddening analysis, shown in orange. The gray regions are not examined by the method. The dashed green line represents the expected position of the Perseus arm from Choi et al. (2014). HMSFRs from Reid14 and Sakai19 are shown as green dots. In blue we show the stars from Xu et al. (2018) that have parallaxes detected at $>5\sigma$ within this region. A number of features match between the stars and clouds. The clouds, like the stars, do not seem to bear any relation to the arm model, except very near the HMSFRs at $l \sim 140°$ as expected.

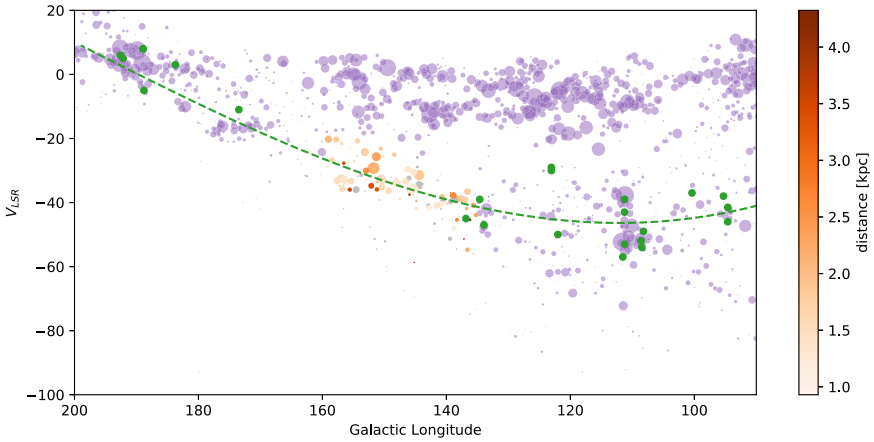

Figure 5. Circles are CO clouds from MML17. The color bar represents the distance found through reddening the analysis. The green dots are Reid14 and Sakai19 HMSFRs. The green dashed line is the Perseus arm model from Choi et al. (2014). Clouds that are very near each other in the longitude–velocity diagram often have very different distances.

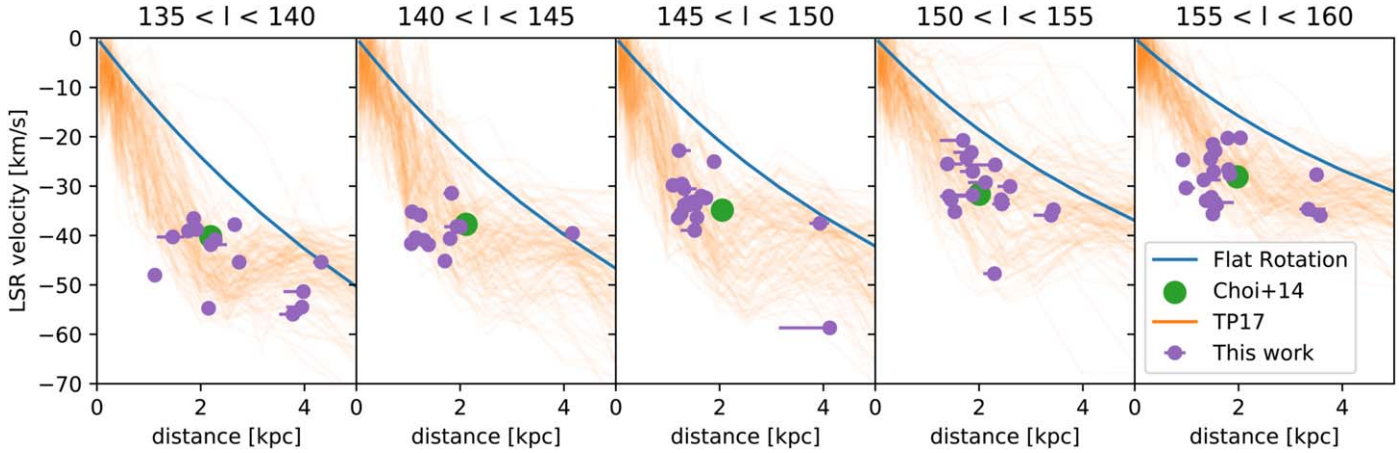

Figure 6. Distance–velocity diagrams for five degree sections of the Galactic plane. The standard 220 km s^{-1} flat rotation curve is shown in blue. The model of the Perseus arm presented in Choi et al. (2014) is shown as a green dot for the central longitude of the region. The orange lines represent the results of TP17. These distance–velocity lines are a grid of samples across the longitude selection and within $-2.^{\circ}5 < b < 2.^{\circ}5$, spaced at $0.^{\circ}5$ intervals. The purple dots and error bars are the results of our analysis presented in Table 1.

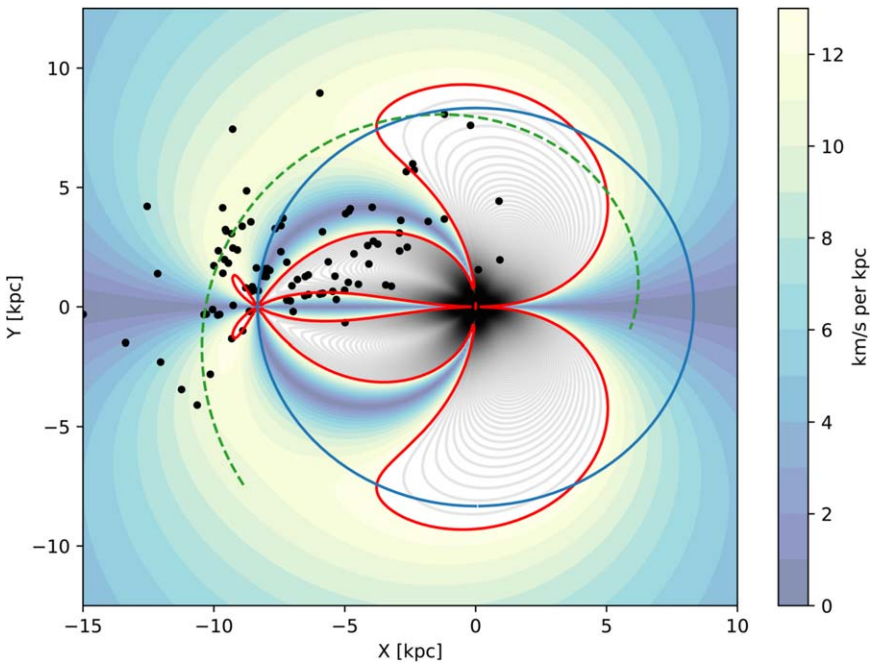

Figure 7. A top-view of the Galactic disk, with the Sun to the left and Galactic center at (0, 0). The arc of the Perseus arm defined in Choi et al. (2014) is shown in green. Regions with a shallower distance–velocity slope expected from a flat rotation curve than that seen toward Perseus shown in color scale and regions with steeper slope shown in grayscale, separated by the red line. Masers from Reid14 are shown in black. Almost all of the outer disk could be impacted at a level similar to the region we consider, as could inner-disk regions near the tangency points and on the far side of the Galaxy. This diagram implies that most connections we draw between masers using the longitude–velocity diagram to form spiral arms are subject to "Burton's Curse".

over this area of sky in the velocity range we are examining. At velocities above about -30 km s^{-1}, the TP17 curves show a distance consistently closer than the purported track of the Perseus arm, with velocities closer to zero typically closer to the Sun; at lower velocities, there is essentially no consistently measurable relationship between the distance and velocity.

To understand the scope of the problem, this effect presents our disk-mapping efforts across the whole of the disk; we chart the steepness of the distance–velocity relationship for an assumed flat, 220 km s^{-1} disk in Figure 7. The red line shows the boundary of 13 km s^{-1} kpc^{-1}, about the steepest expected gradient in the region where we see a velocity crowding effect generate the illusion in the longitude–velocity diagram. This map shows that nearly the entire outer Galaxy and about half of the inner Galaxy are susceptible to these illusory features given bulk flows of the scale seen toward Perseus. This provides a serious warning to investigators using the longitude–velocity diagram to link star-forming features in large swathes of the Milky Way disk.

5. Conclusion

In this work, we have shown that, as originally proposed in B71, real velocity deviations from a flat Galactic rotation curve can a have significant impact on our ability to discern spiral structure in the Galactic longitude–velocity diagram (Figure 1). In particular, we demonstrated that the longitude–velocity bridge of molecular gas connecting the star-forming regions at $l = 135^{\circ}$ and $l = 180^{\circ}$ is entirely an artifact of these velocity

deviations (Figure 4). The amplitude of these velocity variations can create confusion in the longitude–velocity diagram for the bulk of the Galactic disk (Figure 7).

We believe these results have significant implications for the study of the Galactic structure. On the smaller scale, the Perseus arm is often used as a proving ground for theories of star formation. This work shows that one cannot simply lump gas together at Perseus arm velocities in the second quadrant and expect to be probing only a spiral arm; gas at the Perseus arm velocity can extend over at least 3 kpc in the radial distance. On larger scales, we believe this work implies that Galactic spiral arm identification, especially when many discrete star-forming regions are connected using the longitude–velocity diagram, requires true 3D evidence. Luckily, recent dust tomography work (e.g., G19) has been able to probe gas out to many kpc from the Sun. To extend this work, and reveal the true spiral structure of the Galaxy, we will need even deeper observations and more sophisticated stellar and dust inferences schema. We hope this motivates the pursuit of deep and precise observations by upcoming large-angle imaging surveys, such as those conducted with the Vera Rubin Observatory and the Nancy Grace Roman Space Telescope.

This work was supported in part by the US National Science Foundation under grant 1616177. The authors thank Eddie Schlafly, who originally pointed out the lack of a continuous Perseus arm in the 3D dust data. The authors profusely thank Bob Benjamin for long discussions, guidance, and wisdom without which this work would not have been possible. The authors acknowledge Paris-Saclay University's Institut Pascal programs "The Self-Organized Star Formation Process" and "The Grand Cascade" and the Interstellar Institute for hosting discussions that nourished the development of the ideas behind this work. The authors thank the anonymous referee whose report has significantly enhanced this work.

Appendix
Corrected and Augmented Version of the MML17 Molecular Clouds Catalog

The analysis in this paper relies on a corrected version of the molecular cloud catalog of Miville-Deschênes et al. (2017b).

A.1. Astrometry Error Correction

An error in the coordinates of the cloud catalog published in MML17 has been identified after publication: GLAT is offset by one beam (7.′5), and the central velocity is offset by one channel (1.3 km s^{-1}). Correcting this astrometry error resulted in a slight increase in the number of clouds for which a kinematic distance could be estimated, from 8107 to 8246 clouds. The current study uses this corrected version of the catalog.

A.2. Extended Products

The original catalog provided in MML17 contains only clouds for which a kinematic distance could be estimated. These clouds correspond to 89% of the total CO emission, while the whole cloud data set contains 98% of the emission. To extend the original product we are providing a catalog that contains the full set of 9710 clouds that encapsulate 98% of the ^{12}CO (J = 1-0) emission. Clouds for which a kinematic distance could not be estimated do not have mass, density, or physical size estimates.

In addition to this extended cloud catalog, we used the full set of Gaussian components used to describe the ^{12}CO emission of the Milky Way disk to compute a series of extended products. These include

1. The whole Gaussian data set used to described the CO emission.
2. All 9710 reconstructed CO emission position-position–velocity cubes, one per cloud.
3. 2D maps of the number of clouds and the number of Gaussian on each line of sight.
4. A cube providing the list of Cloud ID at each sky position.
5. A reconstruction of the whole ^{12}CO data cube, only based on the Gaussian components.

All these products are publicly available on Dataverse at https://doi.org/10.7910/DVN/QR9CFW.

ORCID iDs

J. E. G. Peek https://orcid.org/0000-0003-4797-7030
Kirill Tchernyshyov https://orcid.org/0000-0002-7351-6062
Marc-Antoine Miville-Deschenes https://orcid.org/0000-0002-7351-6062

References

Bolatto, A. D., Wolfire, M., & Leroy, A. K. 2013, ARA&A, 51, 207
Burton, W. B. 1971, A&A, 10, 76
Burton, W. B., & Bania, T. M. 1974, A&A, 33, 425
Choi, Y. K., Hachisuka, K., Reid, M. J., et al. 2014, ApJ, 790, 99
Dame, T. M., Hartmann, D., & Thaddeus, P. 2001, ApJ, 547, 792
Efron, B. 1982, in CBMS-NSF Regional Conference Series in Applied Mathematics (Philadelphia, PA: SIAM)
Green, G, M. 2018, JOSS, 3, 695
Gaia Collaboration, Brown, A. G. A., Vallenari, A., et al. 2018, A&A, 616, A1
Gaia Collaboration, Brown, A. G. A., Vallenari, A., et al. 2021, A&A, 649, A1
Green, G. M., Schlafly, E., Zucker, C., Speagle, J. S., & Finkbeiner, D. 2019, ApJ, 887, 93
Hall, P. 1985, Stoch. Process. their Appl., 20, 231
Humphreys, R. M. 1976, ApJ, 206, 114
Kalberla, P. M. W., Burton, W. B., Hartmann, D., et al. 2005, A&A, 440, 775
Kalberla, P. M. W., & Kerp, J. 2009, ARA&A, 47, 27
Levine, E. S., Blitz, L., & Heiles, C. 2006, ApJ, 643, 881
Lin, C. C., Yuan, C., & Shu, F. H. 1969, ApJ, 155, 721
Majewski, S. R., Schiavon, R. P., Frinchaboy, P. M., et al. 2017, AJ, 154, 94
Miville-Deschênes, M.-A., Murray, N., & Lee, E. J. 2017a, ApJ, 834, 57
Miville-Deschênes, M.-A., Salomé, Q., Martin, P. G., et al. 2017b, A&A, 599, A109
Pantaleoni González, M., Maíz Apellániz, J., Barbá, R. H., & Reed, B. C. 2021, MNRAS, 504, 2968
Poggio, E., Drimmel, R., Cantat-Gaudin, T., et al. 2021, A&A, 651, A104
Reid, M. J., Menten, K. M., Brunthaler, A., et al. 2014, ApJ, 783, 130
Roberts, W. W. J. 1972, ApJ, 173, 259
Sakai, N., Reid, M. J., Menten, K. M., Brunthaler, A., & Dame, T. M. 2019, ApJ, 876, 30
Schlafly, E. F., Green, G., Finkbeiner, D. P., et al. 2014, ApJ, 789, 15
Sellwood, J. A., & Carlberg, R. G. 1984, ApJ, 282, 61
Sellwood, J. A., & Masters, K. L. 2021, arXiv:2110.05615
Sparke, L. S., & Dodd, R. J. 1978, MNRAS, 182, 1
Tchernyshyov, K., & Peek, J. E. G. 2017, AJ, 153, 8
Tchernyshyov, K., Peek, J. E. G., & Zasowski, G. 2018, AJ, 156, 248
Toomre, A. 1981, Structure and Evolution of Normal Galaxies, 111 (Cambridge: Cambridge Univ. Press), 111
van de Hulst, H. C., Muller, C. A., & Oort, J. H. 1954, BAN, 12, 117
Wouterloot, J. G. A., & Habing, H. J. 1985, A&A, 151, 297
Xu, Y., Bian, S. B., Reid, M. J., et al. 2018, A&A, 616, L15
Zasowski, G., Menard, B., Bizyaev, D., et al. 2015, ApJ, 798, 35
Zucker, C., Speagle, J. S., Schlafly, E. F., et al. 2020, A&A, 633, A51